

ARTICLE OPEN

Biocompatible, large-format, inkjet printed heterostructure MoS₂-graphene photodetectors on conformable substratesRidwan F. Hossain¹, Isaac G. Deaguero², Thomas Boland² and Anupama B. Kaul^{1,3} 

An inkjet printed, biocompatible, heterostructure photodetector is described that was constructed using inks of photo-active molybdenum disulfide (MoS₂) and electrically conducting graphene which facilitated charge collection of the photocarriers. The importance of such devices stems from their potential utility in age-related-macular degeneration, which is a condition where the photosensitive retinal tissue degrades with aging, eventually compromising vision. The absence of effective therapeutic remedies for patients with this disorder has motivated the development of such devices to restore some degree of visual function. Inkjet printed, flexible prosthetic devices offer design simplicity where additive manufacturing can enable large format, low-cost arrays. The biocompatible inkjet printed two-dimensional heterojunction devices were photoresponsive to broadband incoming radiation in the visible regime, and the photocurrent I_{ph} scaled proportionally with the incident light intensity, exhibiting a photoresponsivity $R \sim 0.30$ A/W. This is 10^3 times higher compared to prior reports, and detectivity D was calculated to be $\sim 3.6 \times 10^{10}$ Jones. Strain-dependent measurements were also conducted with bending, indicating the feasibility of such devices printed on flexible substrates. Drop cast and printed CT-MoS₂ inks were characterized using techniques, such as Raman spectroscopy, photoluminescence measurements and scanning electron microscopy. Both mouse embryonic fibroblast and human esophageal fibroblast were used for the biocompatibility analysis for inks drop cast on two types of flexible substrates, polyethylene terephthalate and polyimide. The biocompatibility of inks formed using two-dimensional graphene and MoS₂ on polyimide substrates was extremely high, in excess of 98% for mouse embryonic fibroblast.

npj 2D Materials and Applications (2017)1:28; doi:10.1038/s41699-017-0034-2

INTRODUCTION

Retinal degenerative diseases such as age-related macular degeneration (AMD) and retinitis pigmentosa result in a continuous degeneration of photoreceptors in the retina which eventually leads to complete blindness.^{1, 2} The photoreceptor layer of the retina malfunctions while the inner nuclear layer and the ganglion cells remain fully functional. Pharmaceutical treatments have been developed in an attempt to slow down tissue degeneration, but no method to halt or completely retard the progression has been successfully developed.³ Retinal prosthetic devices may be viable as a vision-recovery methodology to restore vision through electrical stimulation.^{4, 5} Another approach to combat AMD is via the use of artificially implantable photodetectors that are physically placed on the retina. This approach, while promising, suffers from issues of Si substrate rigidity,^{6, 7} where retinal cells migrate to fill the empty space between the implant and retinal pigment epithelium (RPE), which leads to the formation of scar tissue and cell reorganization in the various layers of the retina. Having large format photodetector pixels that are flexible and conformable allows the implant to be in intimate contact to RPE,⁸ and alleviates the issues faced with rigid and planar Si implants. Besides this advantage, such conformable structures also have the potential to increase areal coverage where photodetector pixels can be constructed to enhance the field of view by collecting more of the incoming radiation and

focusing it onto the retina, given the naturally curved, hemispherical geometry of the eye.

In this paper, a new approach was utilized to form photo-sensitive pixels that utilize heterostructures of inkjet printed two-dimensional (2D) layered materials, specifically photosensitive and semiconducting molybdenum disulfide (MoS₂) and electrically conducting graphene, using inks that also show a high degree of biocompatibility as gauged via cell proliferation tests. In addition, the biocompatible inks are formed on flexible and conformable substrates using low-cost, additive manufacturing technique, specifically inkjet printing, which increases the likelihood of high-throughput translational opportunities targeted specifically toward AMD. Inkjet printing is a process where pico-liter droplets of ink are ejected onto a substrate in a controlled manner in order to construct macroscale architectures.⁹ In the past, printed sensors have been constructed from graphene based inks¹⁰ while other groups have utilized inkjet printing for printing cells and tissue for biomedical applications.¹¹

Interestingly, 2D materials have recently received tremendous attention due to their unique properties and their potential in various types of nanodevices.^{12, 13} The layered structure of MoS₂ is similar to graphene, but unlike the absence of a band gap in graphene, MoS₂ evolves from an indirect band gap semiconductor toward direct band gap for monolayers, as deciphered from Raman and photoluminescence measurements.^{14, 15} While the photonic and optoelectronic properties of 2D materials are being

¹Electrical and Computer Engineering, University of Texas at El Paso, El Paso, TX 79968, USA; ²Metallurgical, Materials and Biomedical Engineering, University of Texas at El Paso, El Paso, TX 79968, USA and ³Department of Materials Science and Engineering; Department of Electrical Engineering, University of North Texas, Denton, TX 76207, USA
Correspondence: Anupama B. Kaul (akaul@utep.edu) (Anupama.Kaul@unt.edu)

Received: 11 December 2016 Revised: 21 July 2017 Accepted: 26 July 2017

Published online: 07 September 2017

intensively investigated,^{16, 17} their implementation to biosensing and biomedical applications is limited thus far, although some reports have emerged recently.^{18, 19} Given that these materials exhibit a weak interlayer bonding through the van der Waals interaction, solvents and mild agitation through sonication allows layer separation into monolayer or few-layer nanomembranes from the bulk crystal.²⁰

To advance the utility of these materials for biosensing and biomedical applications, the biocompatibility of 2D graphene and MoS₂ with both mouse embryonic fibroblasts (STO) and human esophageal fibroblasts (HEF) cell lines was explored, for photodetector applications with potential for retinal prostheses. Whether being used for implantable sensors, chips, drug delivery, or cell imaging purposes, the biocompatibility of nanomaterials is paramount for in vivo applications to alleviate cytotoxicity effects and minimize the immune response. Cytotoxicity of MoS₂ nanosheets has been analyzed via electrical impedance measurements using rat pheochromocytoma cells (PC12) and rat adrenal medulla endothelial cells.²¹ Cytotoxicity of graphene oxide and graphene sheets also has been investigated by measuring mitochondrial activity in adherent human skin fibroblasts using in vitro hemolysis and WST-8 viability assays.²² In addition, cytotoxicity associated with metal-oxide nanoparticles such as ZnO, CuO, and TiO₂ with human alveolar basal epithelial (A549) cells showed a time-dependent response,²³ while other reports discuss the adsorption and accumulation of gold nanoparticles in swine organs that exhibited minimal hematological or renal side effects.²⁴

In this work, both drop cast and printed CT-MoS₂ ink were characterized using Raman spectroscopy, photoluminescence (PL) measurements and scanning electron microscopy (SEM). Two flexible substrates, polyethylene terephthalate (PET) and polyimide, were used as the templates upon which to construct the photodetectors and assess their biocompatibility. Confocal microscopy was used to gauge the degree of biocompatibility of all of the formulated dispersions after the inks were exposed to two different cell lines, STO and HEF. Besides analyzing the photoresponse of the devices and the biocompatibility of ink formulations, strain-dependent bending tests were also conducted that showed the modulation of the photocurrent as a function of strain, where the devices were still photoresponsive over large strain levels. This work shows the important first steps toward the successful realization of prototype "all" inkjet printed 2D heterostructure photodetector devices, that should pave the way for their future implementation in retinal prosthesis and AMD.

RESULTS AND DISCUSSION

Biocompatibility analysis

The graphene and MoS₂ ink was obtained via sonication using three different solvents, isopropyl alcohol (IPA), a mixture of cyclohexanone/terpineol (C/T) at a ratio of 7:3, and N-methyl-2-pyrrolidone (NMP), resulting in six separate inks: IPA-Graphene; C/T-Graphene; NMP-Graphene; IPA-MoS₂; C/T-MoS₂; and NMP-MoS₂. A comprehensive biocompatibility analysis was performed with STO and HEF cell lines by exposing the graphene and MoS₂ samples with cells for 72 h using a set up shown in Fig. 1a; further details on the experimental procedures are provided in the "Methods" section.

Given that PET is widely accepted as a biocompatible material,^{25, 26} this exploration began with PET as the initial starting substrate. Figure 1b, c is an example of the IPA-Graphene and C/T-Graphene ink drop cast onto PET substrates, where biocompatibility tests were conducted using the STO cell line. The red-bordered regions in Fig. 1b show a large cell-free zone where no cells are seen to proliferate. In Fig. 1c, a small solid deposit of the C/T-Graphene ink also clearly shows a cell-free zone where no

cells grow close to the 2D material deposit. Shown in Fig. 1d is a light microscopy image of the C/T-MoS₂ ink, which also depicts a large cell-free zone, where proliferation is low or nonexistent, which is also corroborated by the confocal microscopy image in Fig. 1e; here the regions marked in red represents dead cells, and the green colored regions are indicative of live cells. The biocompatibility results of 2D inks using PET substrates were initially very surprising, where cell proliferation seemed non-existent or prohibited for both MoS₂ and graphene using inks composed of relatively mild solvents such as IPA and C/T. However, this lack of biocompatibility can be explained on the basis of the process used to form inks on PET. The relatively low ~260°C melting point of the PET substrates restricted the use of baking temperatures above ~100°C where material softening is known to occur. This low baking temperature used has the potential to trap remnant solvents in the deposited material, which creates a harsher environment for cells in the immediate vicinity, as seen from the data in Fig. 1b–e. Vacuum annealing used in the past²⁷ may be an effective way to drive off the entrapped solvents on PET substrates which we will explore in more detail in the future.

With the negative biocompatibility results obtained using PET, an alternate substrate, specifically polyimide was investigated. Figure 2a–f represents the optical microscopy images of drop cast graphene and MoS₂ samples on polyimide, respectively, where the regions near the deposited 2D ink are clearly surrounded by STO. These samples appear more biocompatible, as their elongated morphology indicates their healthy nature, and the absence of a cell-free zone suggests the favorable conditions for cell proliferation. The STO cell confluence rate was calculated using a hemocytometer, and percentages were based on the amount of cells present in the control wells, where the cells were cultured in the absence of the drop cast sample and in the presence of media [Dulbecco's modified Eagle's medium (DMEM) with 10% fetal bovine serum (FBS) and 1% antibody; details can be found in the "Methods" section]. When analyzing any of the solvents, IPA, C/T or NMP with polyimide substrates, both graphene and MoS₂ resulted in a confluence rate of 70–98%, in contrast to PET samples where the confluence rate was much lower, 15–60%, as shown by the data in Fig. 2g; Fig. 2g provides a comparative analysis of the MoS₂ and graphene on both PET and polyimide substrates. Moreover, wells containing MoS₂ on the polyimide film had a large number of cells growing on the polyimide substrate itself, further indicating its high biocompatibility. It is important to take note that while calculating the confluence rate, the volume taken by the sample itself could be potentially populated by the cells but this volume was small and may increase the confluence results in Fig. 2g by a negligible fraction ~0.05%. The high degree of biocompatibility seen for the 2D MoS₂ and graphene inks, even for a harsh solvent such as NMP, is likely due to the higher annealing temperature of 330 °C used for the polyimide substrates, and allowed the effective evaporation of the remnant solvent, which yielded a higher cell confluence rate, as observed.

To analyze the results on the polyimide substrates further, confocal microscopy was used to gauge the degree of biocompatibility for all of the formulated dispersions. Figure 3a–f depicts a confocal microscopy image of IPA, C/T and NMP with both graphene and MoS₂ samples for the STO cell line. Again, the green zone indicates live cells while the red zone represents dead cells. The control showed a natural dead cell count of ~1% which is not surprising and is within the natural attrition rate of STO cells. The confocal image indicates a very small, near negligible dead cell count compared to the STO cell line, and suggests a high degree of biocompatibility of the 2D inks using a human cell line. The data from the STO cell line were analyzed in further detail by mapping the confocal image to *ImageJ* software from which the percentage of the live-to-dead cells was computed for all six samples, as

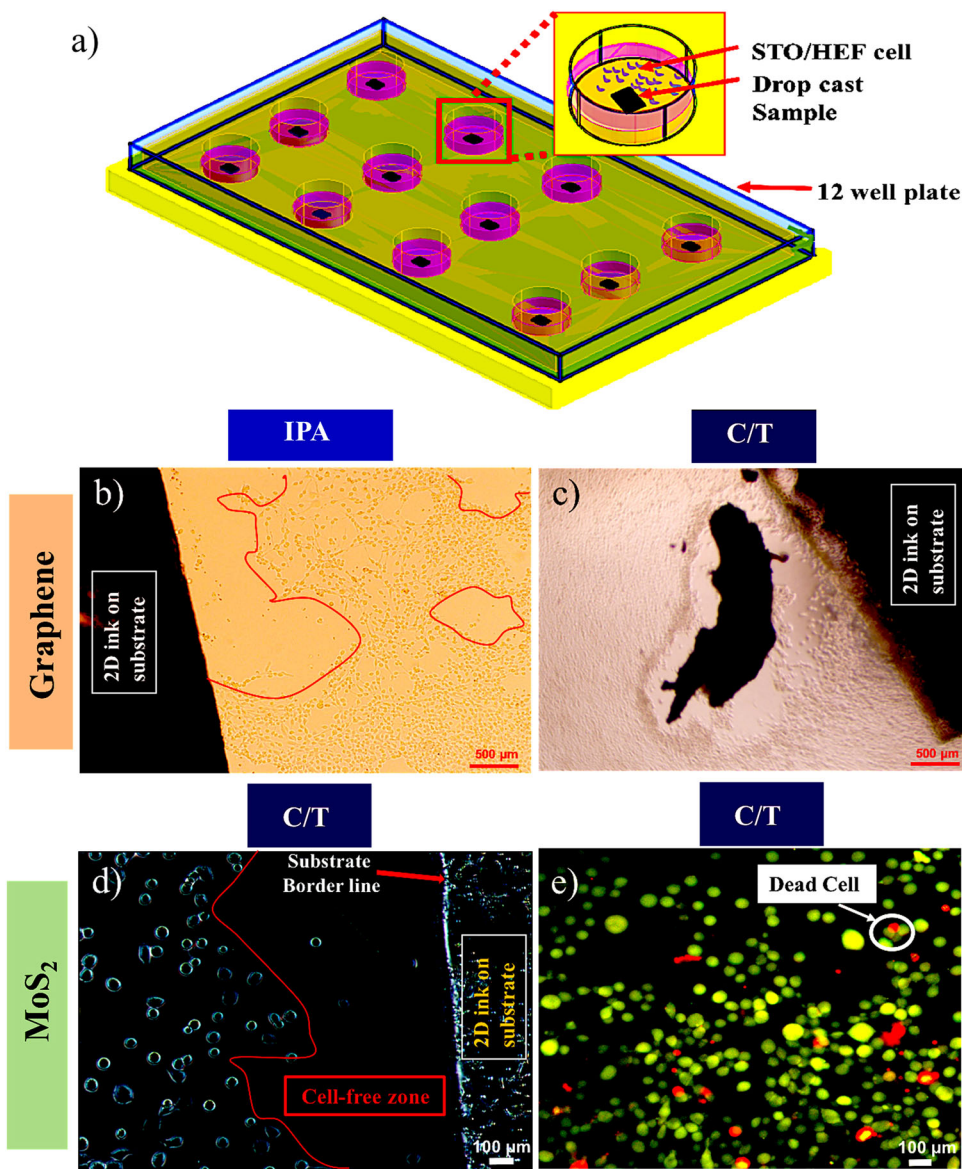


Fig. 1 **a** Schematic diagram showing the set up used for the biocompatibility tests with a 12-well plate, where incubated STO/HEF cell lines were used. The drop cast 2D materials are shown in the *top right inset* on the respective substrate. Results in **b–e** show biocompatibility analysis for PET substrates; **b** Optical microscopy showing a large patch of cell-free zone when IPA-Graphene is drop cast on PET. **c** A solid deposit of the C/T-Graphene on the PET also shows a clear cell-free zone region in the vicinity of the substrate. **d** Light microscopy showing a large border cell-free zone where cell proliferation is low or nonexistent in the C/T-MoS₂ sample. **e** Confocal image showing a significant fraction of dead cells for C/T-MoS₂ sample; here *red* represents dead cells and the *green* regions are live cells. For PET substrates, both graphene and MoS₂ showed less cell confluence for all the solvents tested

shown in Fig. 3g. The NMP samples, with both graphene and MoS₂, showed a higher percentage of dead cells, ~5–7% compared to the other two solvents, which is not surprising given the inherently toxic nature of NMP that served as a negative control. However, the C/T and IPA dispersions yielded a dead cell ratio <5%. Thus, the results from the NMP dispersion suggest that there may still be a small amount of solvent retained within the samples. The *inset* in Fig. 3h depicts the converted 8-bit image from which the total number of cells was calculated to be ~716 in this particular case.

To diversify the biocompatibility analysis, the biocompatibility measurements were also conducted using another cell line, specifically the HEF, in addition to the STO. These tests of HEF also showed promising results with high levels of cell proliferation, and an elongated, healthy cell morphology, suggestive of good cell health. This is evident from the images shown in Fig. 4, which

displays both the (a) optical and (b) confocal images of IPA-MoS₂ and C/T-MoS₂ ink, respectively, for exposure to the HEF cell line. Dead cell percentage was also analyzed for the HEF cell line where the C/T and IPA dispersions yielded a dead cell count of <3%.

Nonetheless, the high degree of biocompatibility of graphene and MoS₂ inks using polyimide substrates was further developed to integrate these inks into photodetector heterostructure architectures. The cytotoxicity effects of free MoS₂ nanosheets has been investigated by Shah et al.²¹ using *in vitro* techniques where they determined that MoS₂ nanosheets were not capable of mechanically penetrating the cell membrane to induce stresses that lead to cell death. For the application considered here in retinal prosthesis, poly-di-methylsiloxane (PDMS) encapsulation can be used to further restrict the dislodging of MoS₂ nanosheets into the fluidic environments of the body. The biocompatible nature of PDMS is well established,²⁸ and its transparent

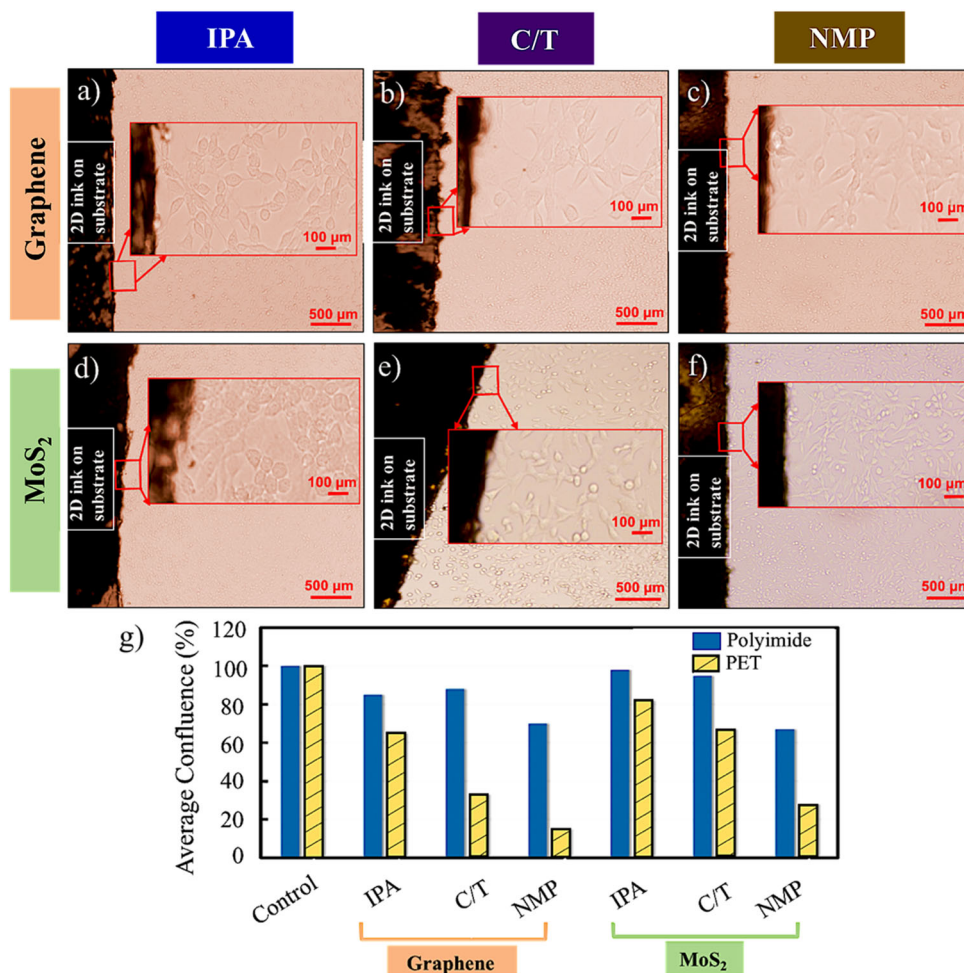


Fig. 2 Biocompatibility analysis of graphene and MoS₂ on polyimide substrates as viewed via optical microscopy measurements for STO. Optical microscopy images for **a** IPA-Graphene, **b** C/T-Graphene, **c** NMP-Graphene, **d** IPA-MoS₂, **e** C/T-MoS₂, **f** NMP-MoS₂. The elongated morphology indicates the healthy, biocompatible nature of all the cells in the case of either graphene or MoS₂ samples. **g** Average confluence percentage for all six samples, which is 15-60% and 70-98% for PET and polyimide samples, respectively

characteristics are also favorable for this application to serve as an ideal encapsulation material for our device in vivo.

Electrical transport of inkjet printed structures and ink characterization

To explore the electrical properties of the dispersions, graphene and MoS₂ inks were first drop cast onto polyimide substrates and annealed at 330 °C for 3 h, after which point the electrical transport properties were measured. The data are shown by the I–V Characteristics in Fig. 5a, b for all six drop cast solutions of graphene and MoS₂. From the I–V Characteristic, it is clear that the graphene sample exhibits an Ohmic response with current levels $I \sim 2$ mA at 1 V for the C/T dispersion, while the MoS₂ samples exhibited nonlinear behavior at low bias voltages, suggestive of a sub-gap region. For all the drop cast samples the distance between the two tungsten (W) probes was ~ 1 mm. Note that the electrical measurements conducted for graphene and MoS₂ on PET substrates yielded electrically insulating 2D inks even up to 20 V, which is likely due to the lower annealing temperature used for these substrates, where a large fraction of the remnant solvent may still be present. From the data in Fig. 5a, b, it is clear that C/T dispersions for both graphene and MoS₂ yielded higher current levels, compared to the other solvents, i.e., NMP and IPA. For this reason, the C/T dispersions was chosen to formulate the

dispersions with rheological properties appropriate for inkjet printing.

In engineering the rheological properties of the C/T ink, ethyl cellulose (EC), a conventional surfactant, was used to achieve a suitable viscosity for inkjet printing. A viscosity of 12 cp is necessary for inkjet printing based on the previous work²⁰ where, in this case, the percentage of EC used was 2.5 wt%. The graphene and MoS₂ inks of C/T were then prepared using techniques discussed in the “Methods” section. Here the 25- μ m thick polyimide film was placed on the platen of the inkjet printer, that was heated to 60 °C and the cartridge temperature was set at 30 °C. For both graphene and MoS₂ inks, 15 passes were printed on the polyimide film, while the print head was cleaned periodically. Then the graphene/MoS₂ printed patterns were annealed at 330 °C for 3 h using the annealing technique described in the “Methods” section. Further details on the printing conditions used are provided in the “Supplemental Information” section.

As shown, for both graphene and MoS₂, C/T enhanced the electronic transport for all of the solvents tested. Further material characterization analysis showed the surface morphology of drop cast C/T-MoS₂ ink gauged using SEM imaging in Fig. 5c, which depicts a platelet size well in excess of 2 μ m, on average. The I–V Characteristic of an inkjet printed pattern is shown in the insets of Fig. 5d for graphene and Fig. 5e for the MoS₂ using the C/T dispersion where the insets at the top show the structure of the

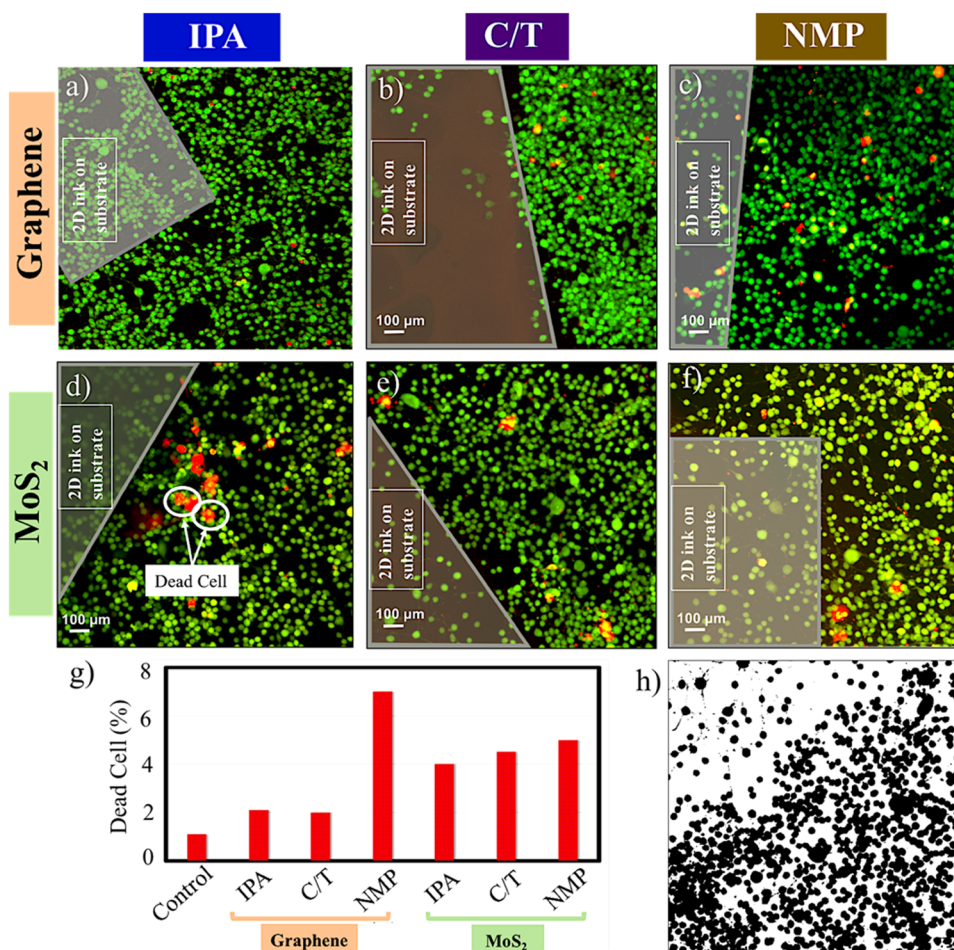


Fig. 3 a–f represents confocal microscopy cytotoxicity assay treated cell images of the polyimide sample for STO, where the specific samples are: **a** IPA-Graphene, **b** C/T-Graphene, **c** NMP-Graphene, **d** IPA-MoS₂, **e** C/T-MoS₂ and **f** NMP-MoS₂. **g** Dead cell percentage of STO cells on polyimide substrates where the data are extracted from confocal images (a–f) using the *ImageJ* software. **h** Converted 8-bit image which was used to calculate the total number of cells, ~716 in this particular case

printed pattern with electrodes. In Fig. 5f the surface morphology of the inkjet printed C/T-MoS₂ is shown using SEM analysis which reveals platelet size to be well below 1 μm , on average, with a packing density that is also higher compared to the drop cast material that will naturally lead to an enhancement in the inter-platelet connectivity compared to the drop cast material as confirmed by the SEM image in Fig. 5c.

Comparing the I–Vs of drop cast and the printed graphene pattern in Fig. 5a, b, d, e, clearly there is an order of magnitude drop in current, and for the printed MoS₂ structures the drop is a mere factor of two. This is to be expected as the thickness of drop cast structures was higher (~10 μm) compared to the printed pattern (~1.9 μm). The thickness values were used to compute the resistivity of drop cast C/T-MoS₂, IPA-MoS₂ and NMP-MoS₂ which was measured to be ~1.7, ~3.7, and ~4.1 k Ω cm, respectively, for the three samples. From this study it is clear that the C/T-MoS₂ dispersion yields enhanced transport across all the three dispersions. In addition, the resistivity of the printed C/T-MoS₂ was found to be ~1.3 k Ω cm, which was less than the resistivity of the drop cast samples. Inkjet printing typically ensures better morphology and inter-membrane connectivity, and thus the conductivity of the printed pattern is higher compared to the drop cast samples as confirmed by the data presented here. On the other hand, the resistivity of drop cast C/T-Graphene, IPA-Graphene and NMP-Graphene was found to be ~10⁴ times lower when compared to the MoS₂ dispersions, with values of ~0.18, ~0.43, and ~1.1 Ω cm, respectively, for the three dispersions.

Incidentally, the resistivity values of MoS₂ measured here are ~10²–10³ times lower when compared to prior reports,²⁷ where the printed MoS₂ resistivity was measured to be ~40 M Ω cm.

It is also well-known that bulk MoS₂ does not exhibit luminescence and has strong direct excitonic absorption at energies much larger than the indirect bandgap. The PL spectra for the drop cast C/T-MoS₂ samples was also measured and the data are shown in Fig. 5g. Equivalently, Fig. 5h shows the PL spectra for the printed C/T-MoS₂ samples. The PL spectra in Fig. 5g did not exhibit any narrow-band luminescence peaks which is an indication that the drop cast C/T-MoS₂ ink is comprised of bulk material.²⁹ Few-layer MoS₂ shows multiple emission peaks which broaden slightly with increasing thickness and systematically shift to lower energies. On the other hand, the PL spectra of the inkjet printed C/T-MoS₂ samples in Fig. 5h indicates two emission bands centered at the Excitonic A peak at ~1.88 eV and the Excitonic B peak at ~1.97 eV, whereas the indirect/peak occurs at 1.29 eV, which is consistent with the notion that the liquid exfoliated MoS₂ membranes are mostly few layers.²⁹

The *top left insets* in Fig. 5g, h display the Raman spectra for the two cases, where the Raman shift $\Delta k \sim 26.5 \text{ cm}^{-1}$ for the drop cast material, while $\Delta k \sim 24 \text{ cm}^{-1}$ for the printed ink; here a 532 nm laser was used for the Raman imaging where measurements were conducted at room temperature. The spectra depict the E_{2g}^1 vibrational mode which appears at $k = 383 \text{ cm}^{-1}$ and represents the in-plane phonon vibrations, while the out-of-plane vibrations are denoted by the A_{1g} mode which is centered at $k = 407 \text{ cm}^{-1}$.

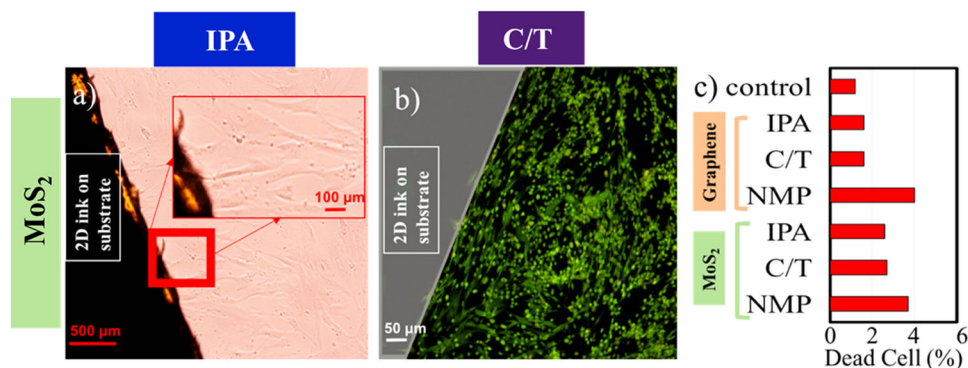


Fig. 4 Biocompatibility analysis on polyimide sample using HEF cell line. **a** Optical microscopy showing high HEF cell confluence for a polyimide IPA-MoS₂ sample. **b** Confocal microscopy image of a polyimide sample C/T-MoS₂ surrounded by HEF. **c** Dead cell percentage of HEF cells on polyimide substrates where the data are extracted from confocal images using the *ImageJ* software

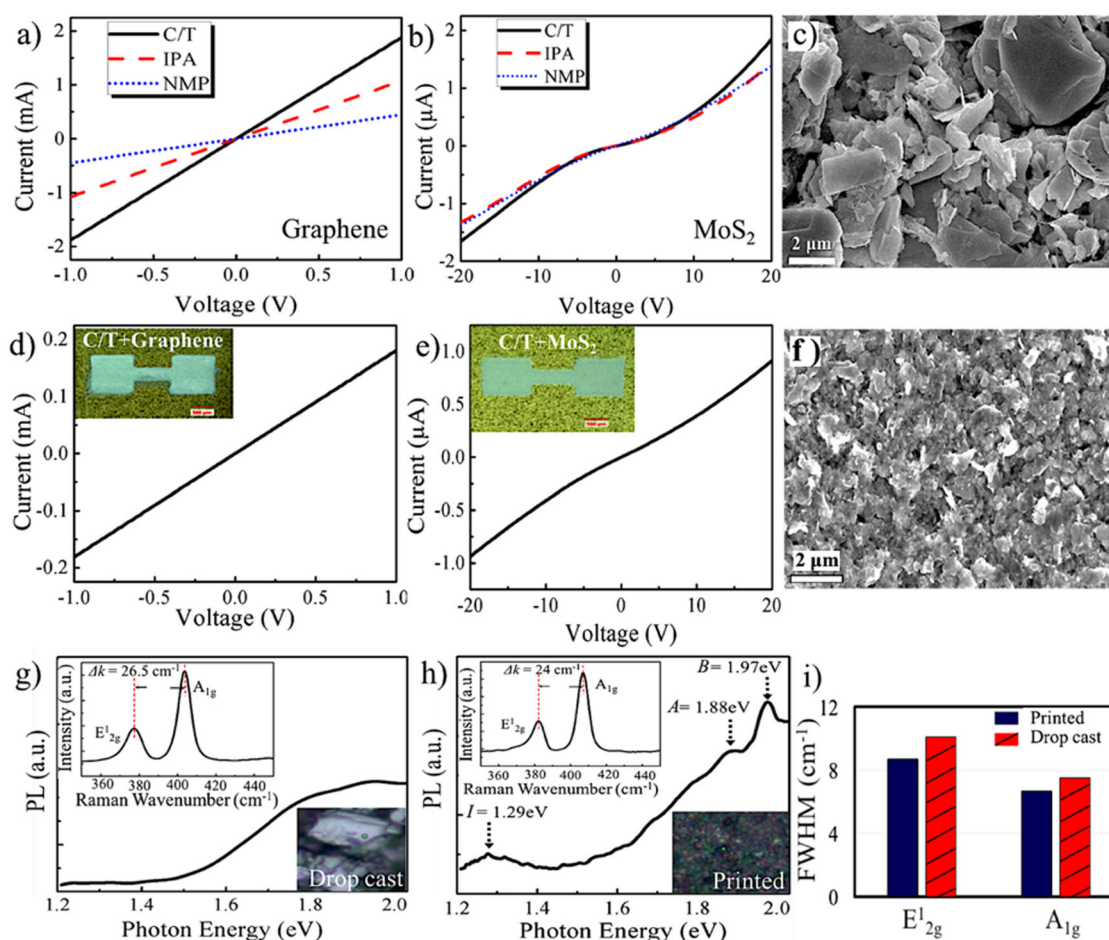


Fig. 5 The I-V Characteristic of drop cast **a** graphene and **b** MoS₂ dispersed in three solvents, IPA, C/T and NMP onto polyimide substrates after annealing. As shown, for both graphene and MoS₂, C/T enhanced electronic transport for all of the solvents tested. **c** Surface morphology of drop cast C/T-MoS₂ ink gauged using SEM imaging which depicts platelet size well in excess of 2 μm, on average. Equivalently, the I-V Characteristic of an inkjet printed pattern shown in the insets of **d** graphene and **e** MoS₂ using the C/T dispersion. **f** Surface morphology of the inkjet printed C/T-MoS₂ where the SEM reveals platelet size to be well below 1 μm on average, and the higher packing density leading to enhanced inter-platelet connectivity compared to the drop cast material in **c**. PL spectra of **g** drop cast C/T-MoS₂ and **h** printed C/T-MoS₂ with the respective imaged regions for PL and Raman shown in the bottom right insets of **g** and **h**; the drop cast sample in **g** did not exhibit any narrow-band luminescence peaks, which is an indication that the drop cast C/T-MoS₂ ink is comprised of bulk material as also noted in Ref. 28. The PL spectra of the inkjet printed C/T-MoS₂ indicates two emission bands centered at the Excitonic A peak at ~1.88 eV and the Excitonic B peak at ~1.97 eV, whereas the indirect/I peak occurs at ~1.29 eV. The top left insets in **g** and **h** display the Raman spectra where the Raman shift $\Delta k \sim 26.5 \text{ cm}^{-1}$ for the drop cast material, while $\Delta k \sim 24 \text{ cm}^{-1}$ for the printed ink. **i** Tabulation of the FWHM for the E_{12g}¹ and A_{1g} peaks from the Raman spectra, indicating the defect densities of the drop cast and printed inks to be comparable, despite the extended duration of sonication in the latter case (48 versus 8 h)

The fact that $\Delta k \sim 26.5 \text{ cm}^{-1}$ for the drop cast material is clearly suggestive of bulk constituents in that dispersion,³⁰ as compared to the inkjet printed material. The *bottom right insets* in Fig. 5g, h show the imaged area that was scanned with the Raman laser. The full-width-half-maximum (FWHM) is also computed for the E'_{2g} and A_{1g} peaks of the Raman spectra, indicating the defect densities to be comparable for the drop cast and the printed inks, despite the enhanced duration of the ultrasonication in the latter case. The drop cast inks were ultrasonicated for 8 h, whereas the ink for printing was ultrasonicated for 48 h, as noted in more detail in the Methods section.

Heterostructure-based photodetector

One of the major advantages of inkjet printing is that different inks can be printed in an additive manner to form heterostructures, with little material waste. The MoS_2 ink was printed on the polyimide film, followed by the graphene ink on top of it. Figure 6a shows the schematic diagram of large format, inkjet printed arrays of heterostructure devices on flexible substrates. Figure 6b displays an array of actual printed devices over a large format ($\sim 60 \times 50 \text{ mm}$) area, where the *inset* on the *right* shows a magnified view of a single heterostructure device. Figure 6c, d exhibits the corresponding photocurrent I_{ph} , photoresponsivity R and detectivity D as a function of the light intensity (mW/cm^2) where a broadband white light source was used. The R and D are important figures of merit for photodetectors, where the R is given in Eq. 1,

$$R = \frac{J_{\text{ph}}}{P_{\text{opt}}} \quad (1)$$

Here J_{ph} is the photocurrent density (A/cm^2), and P_{opt} is in W/cm^2 and refers to the optical power density. The D is tabulated using Eq. 2,

$$D = \frac{A^{1/2} R}{(2qI_d)^{1/2}} \quad (2)$$

where D is measured in $\text{cm Hz}^{1/2}/\text{W}$ (Jones), and A is the effective detector area in cm^2 , I_d is the dark current (A) and q is the electron

charge ($1.6 \times 10^{-19} \text{ C}$). From Eq. 1, the R was calculated to be $\sim 0.30 \text{ A}/\text{W}$ for the inkjet printed heterostructure device, which is $>10^3$ times compared to the other reports of printed heterostructures devices^{31, 32} where WS_2 and MoS_2 and inks were used. The highest D for graphene- MoS_2 heterojunction devices was measured to be $\sim 3.6 \times 10^{10}$ Jones which is comparable to previous reports, where $D \sim 4 \times 10^{10}$ Jones.³³ The photoresponse was measured while illuminating the device with a broadband light source (LEDR/4 type illuminator) which has a color temperature of 6500 K. Both R (Fig. 6c) and D (Fig. 6d) are decreasing with increasing light intensity, but exhibit saturation at higher power density levels, whereas I_{ph} is increasing. The incident light radiation leads to multifaceted mechanisms to arise comprising of carrier generation, separation and transport processes of photo-excited carriers,³⁴ and trap states within the multilayer MoS_2 can also influence the photoresponse at high power densities.³⁵ In some prior reports R as high as $\sim 1 \times 10^4 \text{ A}/\text{W}$ was achieved, however this was for non-solution processed materials where conventional top-down fabrication on silicon substrates was used with Si nanowires.³⁶ The variation of I_{ph} as a function of bias voltage at various light intensities is shown in the *inset* of Fig. 6d. The light intensity was increased up to $18.5 \text{ mW}/\text{cm}^2$ on the photodetector device. At $18.5 \text{ mW}/\text{cm}^2$, $I_{\text{ph}} = 2.1 \mu\text{A}$ (applied bias voltage $\sim 20 \text{ V}$) which showed a near linear increase as light intensity increased. Note that this increase in I_{ph} as a function of light intensity is witnessed in several prior reports where photoconductivity of individual monolayer (or few-layer) MoS_2 has been studied.^{37, 38}

With the incident light, the increase of I_{ph} can easily be explained from the energy band diagram, where electrons from the valence band are excited to the conduction band (CB) through the absorption of incident optical radiation, which increases the concentration of photocarriers. An Ohmic contact is presumed to arise here, where the work function ϕ of graphene $\phi_{\text{graphene}} = 4.5 \text{ eV}$ and lies below the CB edge of MoS_2 , and $\phi_{\text{MoS}_2} = 5.12 \text{ eV}$. Printed MoS_2 ink conductivity σ was also calculated to be $\sim 9 \times 10^{-2} \text{ S}/\text{m}$ at $18.5 \text{ mW}/\text{cm}^2$ which suggests an increase of 10^4 times in σ compared to previous reports for solution-processed MoS_2

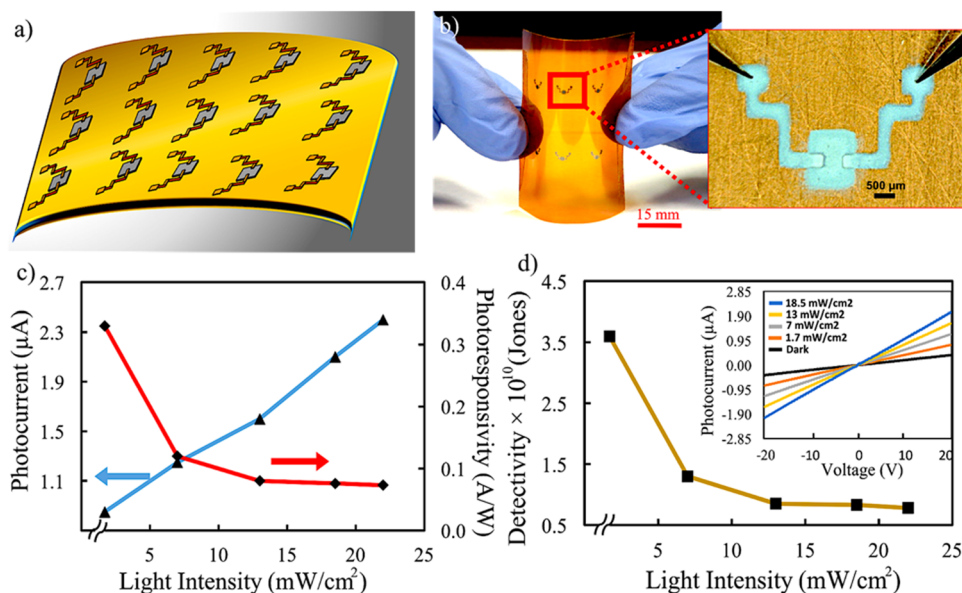


Fig. 6 **a** A design file showing the potential for scalability for printing such 2D heterostructure devices for AMD over a large format using low-cost inkjet printing on flexible substrates. **b** An actual array of inkjet printed heterostructure devices on flexible polyimide film over an area of $60 \times 50 \text{ mm}$. *Inset* image on the *right* depicts a single inkjet printed heterostructure device, where graphene electrodes were printed on top of the MoS_2 layer. **c** The dependence of I_{ph} and R on light intensity at 20V. **d** D as a function of light intensity at 20V. *Inset* shows the I-V Characteristics at various light intensities, where I_{ph} is seen to increase linearly with light intensity

photodetectors that utilized interdigitated graphene electrodes where $\sigma \sim 2.5 \times 10^{-6} \text{ S/m}$ even at light intensities $>18.5 \text{ mW/cm}^2$.²⁷

Strain-dependent photoresponse

To validate the mechanical durability of the photodetectors on the flexible polyimide substrates, mechanical bending tests were carried out using 3D printed structures with five different radii of curvatures: 0.072, 0.087, 0.112, 0.157, 0.262 cm^{-1} . The experiment was performed under a bias voltage of 20 V, and the photocurrent response was measured as a function of strain with varying light intensity.

The flexible heterostructure device was attached to the 3D fixtures as shown in the bottom two *insets* of Fig. 7a for example curvatures of ~ 0.087 and $\sim 0.157 \text{ cm}^{-1}$. Double-sided tape was used for mounting the samples onto the fixtures. The data in Fig. 7a shows the device to be photoresponsive as a function of strain for curvatures of ~ 0.087 , ~ 0.157 and $\sim 0.262 \text{ cm}^{-1}$, though I_{ph} decreased with increasing strain, as expected. The applied strain possibly increases the membrane-to-membrane separation which explains the decrease in I_{ph} with increasing strain, consistent with prior reports that have explored strain dependence of electronic transport properties in other material systems.³⁹ On a flat surface, where curvature = 0 cm^{-1} , the photodetector yielded the highest I_{ph} where maximal charge separation and collection via the graphene electrodes occurs, while increasing curvature reduced the I_{ph} . When the strain is applied, few layer MoS_2 causes the mechanical deformation and produces piezoelectric charges at the heterostructure interface. The electric field at the interface and the increased metal-semiconductor junction provides a smaller driving force to separate photo-generated electron-hole pairs, which reduces I_{ph} . Figure 7b illustrates the dependence of I_{ph} and R captured at a light intensity of $\sim 22 \text{ mW/cm}^2$ as a function of curvature. Also R decreased slightly with the increase in curvature similar to the I_{ph} response.

These biocompatible devices were demonstrated to be photo-responsive which is attractive for flexible electronics generally, but also has a particular significance for flexible and implantable electronics. Implantable devices that currently address retinal degenerative diseases still rely on conventional Si-based implants that utilize thin film fabrication and lithography in expensive cleanroom environments.^{6, 7} Despite the expense, the device feature sizes of Si-implants for retinal prosthesis are $\sim 30 \mu\text{m}$. While the devices described in this work thus far are based on feature sizes $>200 \mu\text{m}$, in Fig. 7c inkjet printed circuitry on flexible polyimide substrates is illustrated in the *inset*, where the achieved line widths are far smaller $\sim 80 \mu\text{m}$ with absolute printed lengths approaching $\sim 20 \text{ cm}$. It can be seen from Fig. 7c that the current scales inversely with increasing probe separation in such structures, as expected. Even though this circuitry is printed with C/T- MoS_2 ink, it translates readily to graphene also, potentially for interconnect applications. Figure 7d shows the optical microscopy image of an array of printed $80 \mu\text{m}$ lines, where the edges show good line resolution from the magnified image on the right. This scaling toward lower line widths using printed 2D materials can be pushed even further by tuning ink-substrate interactions, so the device features are comparable to those used in conventional Si implants for retinal prosthesis.

In this paper, the biocompatibility of 2D materials—graphene and MoS_2 —that were drop cast onto flexible PET and polyimide substrates using mouse embryonic fibroblast (STO) and HEF cell lines was explored. The PET was shown to inhibit cell growth due remnant solvents trapped within the samples, as elucidated through the observance of cell-free zones and minimal cell proliferation. Confocal microscopy was performed to gauge the biocompatibility of the polyimide samples, since the PET samples showed negative biocompatibility results using STO. Polyimide samples for both STO and HEF showed high biocompatibility with a cell survival rate of up to $\sim 98\%$ and a confluence rate of 70-98%. Characterization conducted using SEM imaging, PL and Raman

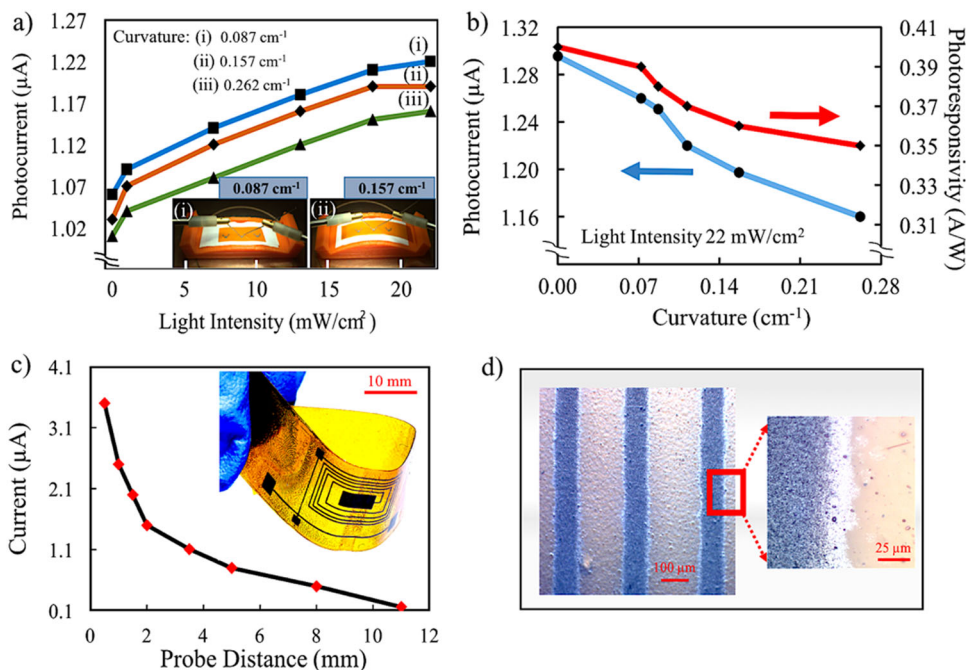


Fig. 7 **a** The relative I_{ph} change as a function of light intensity at curvatures (i) 0.087 cm^{-1} , (ii) 0.157 cm^{-1} , (iii) 0.262 cm^{-1} . The *bottom two insets* depict the 3D printed fixtures used, upon which the devices under test were mounted for the strain-dependent measurements. **b** I_{ph} and R as a function of curvature to gauge the effect of strain at 22 mW/cm^2 . **c** Current versus probe distance data for a printed (C/T- MoS_2) device illustrated in the *top inset*, where the $80 \mu\text{m}$ line widths that span 220 mm illustrate the potential for scalability using 2D inks which can compete with conventional Si-implantable devices for AMD. **d** Optical microscopy image of the printed $80 \mu\text{m}$ line arrays, where the edges show good line resolution from the magnified image on the right

spectroscopy reveals that the inkjet printed C/T-MoS₂ ink has mostly few layer membranes whereas the drop cast C/T-MoS₂ ink is comprised of bulk material. The FWHM was also computed for the E_{12g}^1 and A_{1g} peaks indicating the defect densities to be comparable for the drop cast and printed inks. A biocompatible photodetector on a flexible polyimide substrate was designed, fabricated and tested as a function of light intensity and strain. The device showed a photosensitivity $R \sim 0.30$ A/W which is 10^3 times higher compared to prior reports,^{31, 32} and the detectivity D was $\sim 3.6 \times 10^{10}$ Jones even at a very low light intensities compared to prior reports.³³ This work shows the promising results achieved with graphene and MoS₂ for forming inkjet printed, biocompatible photodetector heterostructures that are responsive to incoming radiation over large strain levels and light intensities. This work will revolutionize and pave the way for the development and implementation of 2D materials for retinal prosthetics. To the best of our knowledge, this is the first such approach that has successfully demonstrated a biocompatible prototype photodetector based on heterostructures of graphene and MoS₂.

METHODS

Cell culture

The passage nine mouse embryonic fibroblasts (STO) was obtained via ATCC (<https://www.atcc.org/>) and was employed to assess the biocompatibility of MoS₂ and graphene dispersions. The graphene and MoS₂ samples were prepared using three different solvents, IPA, C/T and NMP, and then drop cast on either PET or polyimide substrates. The drop cast PET and polyimide samples were annealed at 100 and 330 °C, respectively, for 3 h. The cells were cultured in ~ 75 cm² culture flasks at 37 °C in a humidified incubator by maintaining a 5% CO₂ level. DMEM supplemented with 10% FBS and 1% antibody was used for cell culturing. The cell culture medium was replaced every 24 h until the cells reached a viable confluence of $\sim 80\%$. The cells were then cleaned three times with phosphate-buffered saline (PBS) solution and detached from the flasks using trypsin, and centrifuged to collect the cells and separate them from the trypsin and PBS. The cells were then suspended in a fresh cell growth medium for accurate quantification.

Cell exposure to MoS₂ and graphene substrates

After the substrates were properly annealed, 1 mm squares were placed into a 12-well cell culture plate [FALCON MULTIWELL Tissue Culture Plate]. Figure 1a shows the set up for the biocompatibility tests, where the substrates were attached to the 12-well plate surface surrounded by the STO/HEF cells. Three sets of each material were taped to the bottom of a well and then sanitized under a hood using UV light for 25 min. After this sanitation step, 10,000 cells of STO were placed into each well, along with 200 μ l of DMEM. The 12-well plate was then placed back into the incubator to allow the cells to acclimate with the sample. The DMEM was changed every 24 h, and after 72 h the wells were cleaned three times with PBS, and 200 μ l of pre-warmed cytotoxicity reagent [Marker Gene Technologies Inc. Live:Dead Cytotoxicity Assay Kit] was placed into the wells. The cells were then placed back into the incubator for 30 min. Photographs of the cytotoxicity reagent treated cells were then taken using light and confocal microscopy. Additional three sets of each material were prepared using the same procedure as outlined above, and the DMEM was removed using PBS, which was detached with trypsin and centrifuged individually in 1.5-ml tubes. These cells were then separated from the trypsin and PBS and suspended in 1 ml of fresh media so they could be counted using Trypan Blue and a hemocytometer. The resulting cell counts were then analyzed.

Process of making the inks and the inkjet printing technique

Chemical exfoliation of bulk graphite and MoS₂ powder was used to yield few-layer graphene and MoS₂ nanosheets, and ultrasonication was used in a number of solvents for times of up to 48 h. The specific solvents used for the drop cast sample were: IPA, C/T and NMP. Initial concentrations of surfactant EC in IPA, C/T and NMP were ~ 4 wt%, ~ 2.5 wt% and ~ 6 wt%, respectively, to control the ink viscosity to be in the vicinity of ~ 12 cP for ink jet printing. A concentration of 10 mg/ml of graphene/MoS₂ powder was then added respectively in 10 ml of each solvent. The sonication

temperature was kept under 44 °C by changing the water periodically. The drop cast inks were treated for 8 h, whereas the ink for printing was sonicated for 48 h in a Branson Bath Sonicator (CPX2800) to attain a platelet size more compatible with the printing nozzles in the latter case. A comparison between the membrane sizes of these two formulated inks is shown in Fig. 5c, f. After the initial preparation of the inks, drop casting with a micropipette was used to place a fixed volume of ink onto either polyimide or PET substrates, and the samples were then annealed at ambient atmosphere.

For the printing ink (10 mg/ml graphene/MoS₂ in 10 ml C/T with 2.5 wt% EC), after the first 24 h of sonication, the inks were centrifuged at 1000 rpm for 10 mi to sediment the thicker membranes, and ~ 9 ml of the supernatant was harvested into a new vial. Another 5 mg/ml of graphene/MoS₂ was added to the solution to ensure fewer-layer graphene/MoS₂ membranes are present in the ink, which was followed by another 24 h of ultrasonication. The first centrifugation in this process removes large unexfoliated, bulk materials, while the second addition of the 5 mg/ml allows a higher density of thinner nanomembranes of MoS₂ to be dispersed. The dispersion was kept stable for 24 h to allow sedimentation of the larger particles. Then the 8 ml of supernatant was taken out and placed in a new vial using a regular syringe.

The Dimatix Material Printer (Fujifilm DMP-2831) was used for inkjet printing where a piezoelectric actuation mechanism is used to eject ink droplets, with 16 nozzles which are spaced at 254 μ m with drop size of 10 picoliters. For this experiment, four nozzles were used for printing the material and device structures which resulted in higher printing resolution compared to the case where all 16 nozzles were used; this resulted in non-uniform line edges due to ink spreading on the substrate.⁴⁰

Annealing of drop cast and inkjet printed sample

Annealing is a critical part of the fabrication process in achieving high electrical conductivity from inkjet printed 2D materials for device applications. The annealing of the samples was conducted under ambient pressure conditions without the use of a vacuum oven. For the polyimide samples, the temperature was ramped at a rate of 2.2 °C/min from 70 to 330 °C, with the following time profiles noted at temperatures of 120 and 210 °C. At 120 °C, the sample was baked for 40 min to thermalize the substrate and allow more time for entrapped solvents to diffuse out from the bulk of the material. Similarly, at 210 °C the substrate was held at this temperature for 20 min. Due to the significantly lower softening temperature of PET compared to polyimide, the upper limit for baking the PET substrates was 100 °C where it was held for a duration of 3 h to drive-off as much of the solvent as possible. A ramp rate of ~ 2.2 °C/min was again used from 70 to 100 °C for PET samples. The thickness of the drop cast and inkjet printed material (graphene/MoS₂) was found to be ~ 10 and ~ 1.9 μ m, respectively, through surface profilometry measurements conducted using the Bruker: DektakXT.

Photodetector device fabrication

A heterostructure device with graphene electrodes and a photoactive MoS₂ layer was printed on a flexible polyimide film. A 1-mm square MoS₂ layer was first printed with 15 ink passes and then annealed at ambient environment on a hotplate at 330 °C for 3 h using the approach described in the "Annealing Technique of drop cast and printed sample" of the "Methods" section. After annealing the MoS₂ layer, the printed polyimide film was placed back into the platen at the same (x,y) coordinates to print the next 15 ink passes of the graphene layer and then annealed at ambient atmosphere on a hotplate at 330 °C for 3 h. The two graphene electrodes were 300 μ m wide, with a spacing of 0.5 mm in between them. Identical conditions were used to print and anneal the graphene electrodes. The printed MoS₂ thickness was found to be ~ 1.9 μ m after annealing.

Data availability

The data that support the findings of this study are available upon the request from the Corresponding Author.

ACKNOWLEDGEMENTS

The authors would like to thank Julio Rincon from the Biomedical Device, Delivery, and Diagnostic Laboratory at the University of Texas at El Paso for help with the confocal microscopy. Support is acknowledged from the University of Texas System Faculty Science and Technology Acquisition and Retention (STARS) award

(EC284802). We also greatly thank the Army Research Office (ARO) (grant number W911NF-15-1-0425) who provided funding that enabled us to pursue this work.

AUTHOR CONTRIBUTIONS

A.B.K. and T.B. conceived the overall project. R.F.H. characterized the properties of the inks and used ink jet printing to design and characterize the photodetector devices formed using the 2D MoS₂ and graphene inks. A.B.K. and R.F.H. analyzed the 2D material and device data and came up with the conclusions. R.F.H. and I.G.D. performed the biocompatibility study of the 2D inks and analyzed the data. All contributed toward the manuscript writing and approved of its content.

ADDITIONAL INFORMATION

Supplementary Information accompanies the paper on the *npj 2D Materials and Applications* website (doi:10.1038/s41699-017-0034-2).

Competing interests: The authors declare that they have no competing financial interests.

Publisher's note: Springer Nature remains neutral with regard to jurisdictional claims in published maps and institutional affiliations.

REFERENCES

1. Age-Related Eye Disease Study Research Group. A randomized, placebo-controlled, clinical trial of high-dose supplementation with vitamins C and E, beta carotene, and zinc for age-related macular degeneration and vision loss: AREDS report no. 8. *Arch. Ophthalmol.* **119**, 1417–1436 (2001).
2. Winter, J. O., Cogan, S. F. & Rizzo, J. F. Retinal prostheses: current challenges and future outlook. *J. Biomater. Sci. Polym. Ed.* **18**, 1031–1055 (2007).
3. Abedi, F., Wickremasinghe, S., Islam, A. F., Inglis, K. M. & Guymer, R. H. Anti-VEGF treatment in neovascular age-related macular degeneration: a treat-and-extend protocol over 2 years. *Retina* **34**, 1531–1538 (2014).
4. Zrenner, E., Stett, A., Weiss, S., Aramant, R. B., Guenther, E., Kohler, K. & Haemmerle, H. Can subretinal microphotodiodes successfully replace degenerated photoreceptors? *Vis. Res.* **39**, 2555–2567 (1999).
5. Zrenner, E. Will retinal implants restore vision? *Science* **295**, 1022–1025 (2002).
6. Chow, A. Y., Pardue, M. T., Chow, V. Y., Peyman, G. A., Liang, C., Perlman, J. I. & Peachey, N. S. Implantation of silicon chip microphotodiode arrays into the cat subretinal space. *IEEE Trans. Neural Syst. Rehabil. Eng.* **9**, 86–95 (2001).
7. Wang, L., Mathieson, K., Kamins, T. I., Loudin, J. D., Galambos, L., Goetz, G. & Harris, J. S. Photovoltaic retinal prosthesis: implant fabrication and performance. *J. Neural Eng.* **9**, 046014 (2012).
8. Seo, J. M., Kim, S. J., Chung, H., Kim, E. T., Yu, H. G. & Yu, Y. S. Biocompatibility of polyimide microelectrode array for retinal stimulation. *Mater. Sci. Eng. C* **24**, 185–189 (2004).
9. Calvert, P. Inkjet printing for materials and devices. *Chem. Mater.* **13**, 3299–3305 (2001).
10. Huang, L., Huang, Y., Liang, J., Wan, X. & Chen, Y. Graphene-based conducting inks for direct inkjet printing of flexible conductive patterns and their applications in electric circuits and chemical sensors. *Nano Res.* **4**, 675–684 (2011).
11. Xu, T., Jin, J., Gregory, C., Hickman, J. J. & Boland, T. Inkjet printing of viable mammalian cells. *Biomaterials* **26**, 93–99 (2005).
12. Novoselov, K. S., Geim, A. K., Morozov, S. V., Jiang, D., Zhang, Y., Dubonos, S. V. & Firsov, A. A. Electric field effect in atomically thin carbon films. *Science* **306**, 666–669 (2004).
13. Kaul, A. B. Two-dimensional layered materials: Structure, properties, and prospects for device applications. *J. Mater. Res.* **29**, 348–361 (2014).
14. Splendiani, A., Sun, L., Zhang, Y., Li, T., Kim, J., Chim, C. Y. & Wang, F. Emerging photoluminescence in monolayer MoS₂. *Nano. Lett.* **10**, 1271–1275 (2010).
15. Mak, K. F., Lee, C., Hone, J., Shan, J. & Heinz, T. F. Atomically thin MoS₂: a new direct-gap semiconductor. *Phys. Rev. Lett.* **105**, 136805 (2010).
16. Mak, K. F. & Shan, J. Photonics and optoelectronics of 2D semiconductor transition metal dichalcogenides. *Nat. Photonics* **10**, 216–226 (2016).
17. Fadil, D., Hossain, R. F., Saenz, G. A. & Kaul, A. B. On the chemically-assisted excitonic enhancement in environmentally-friendly solution dispersions of two-dimensional MoS₂ and WS₂. *J. Mater. Chem. C*. doi:10.1039/C7TC01001J (2017).
18. Zhu, C., Du, D. & Lin, Y. Graphene-like 2D nanomaterial-based biointerfaces for biosensing applications. *Biosens. Bioelectron.* **89**, 43–55 (2017).
19. Sarkar, D., Liu, W., Xie, X., Anselmo, A. C., Mitragotri, S. & Banerjee, K. MoS₂ field-effect transistor for next-generation label-free biosensors. *ACS Nano* **8**, 3992–4003 (2014).

20. Michel, M., Desai, J. A., Biswas, C. & Kaul, A. B. Engineering chemically exfoliated dispersions of two-dimensional graphite and molybdenum disulfide for ink-jet printing. *Nanotechnology* **27**, 485602 (2016).
21. Shah, P., Narayanan, T. N., Li, C. Z. & Alwarappan, S. Probing the biocompatibility of MoS₂ nanosheets by cytotoxicity assay and electrical impedance spectroscopy. *Nanotechnology* **26**, 315102 (2015).
22. Liao, K. H., Lin, Y. S., Macosko, C. W. & Haynes, C. L. Cytotoxicity of graphene oxide and graphene in human erythrocytes and skin fibroblasts. *ACS Appl. Mater. Interfaces* **3**, 2607–2615 (2011).
23. Seiffert, J. M., Baradez, M. O., Nischwitz, V., Lekishvili, T., Goenaga-Infante, H. & Marshall, D. Dynamic monitoring of metal oxide nanoparticle toxicity by label free impedance sensing. *Chem. Res. Toxicol.* **25**, 140–152 (2011).
24. Niidome, T., Yamagata, M., Okamoto, Y., Akiyama, Y., Takahashi, H., Kawano, T. & Niidome, Y. PEG-modified gold nanorods with a stealth character for in vivo applications. *J. Control. Release* **114**, 343–347 (2006).
25. Seitz, H., Marlovits, S., Schwendenwein, I., Müller, E. & Vecsei, V. Biocompatibility of polyethylene terephthalate (Trevira® hochfest) augmentation device in repair of the anterior cruciate ligament. *Biomaterials* **19**, 189–196 (1998).
26. Seitz, H., Marlovits, S., Schwendenwein, I., Vecsei, V. & Losert, U. Biocompatibility of polyethylene terephthalate–PET–(Trevira strong)–an in vivo study of the sheep knee. *Biomed. Tech. (Berl.)* **41**, 178–182 (1996).
27. Finn, D. J., Lotya, M., Cunningham, G., Smith, R. J., McCloskey, D., Donegan, J. F. & Coleman, J. N. Inkjet deposition of liquid-exfoliated graphene and MoS₂ nanosheets for printed device applications. *J. Mater. Chem. C* **2**, 925–932 (2014).
28. Hwang, G. T., Im, D., Lee, S. E., Lee, J., Koo, M., Park, S. Y. & Lee, K. J. In vivo silicon-based flexible radio frequency integrated circuits monolithically encapsulated with biocompatible liquid crystal polymers. *ACS Nano* **7**, 4545–4553 (2013).
29. Splendiani, A., Sun, L., Zhang, Y., Li, T., Kim, J., Chim, C. Y. & Wang, F. Emerging photoluminescence in monolayer MoS₂. *Nano. Lett.* **10**, 1271–1275 (2010).
30. Liang, L. & Meunier, V. First-principles Raman spectra of MoS₂, WS₂ and their heterostructures. *Nanoscale* **6**, 5394–5401 (2014).
31. Withers, F., Yang, H., Britnell, L., Rooney, A. P., Lewis, E., Felten, A. & Kim, Y. J. Heterostructures produced from nanosheet-based inks. *Nano. Lett.* **14**, 3987–3992 (2014).
32. Li, J., Naiini, M. M., Vaziri, S., Lemme, M. C. & Östling, M. Inkjet Printing of MoS₂. *Adv. Funct. Mater.* **24**, 6524–6531 (2014).
33. Mukherjee, S., Maiti, R., Katiyar, A. K., Das, S. & Ray, S. K. Novel colloidal MoS₂ Quantum dot heterojunctions on silicon platforms for multifunctional optoelectronic devices. *Sci. Rep.* **6**, 29016 (2016).
34. Konstantatos, G., Badioli, M., Gaudreau, L., Osmond, J., Bernechea, M., De Arquer, F. P. G. & Koppens, F. H. Hybrid graphene-quantum dot phototransistors with ultrahigh gain. *Nat. Nanotechnol.* **7**, 363–368 (2012).
35. Lopez-Sanchez, O., Lembke, D., Kayci, M., Radenovic, A. & Kis, A. Ultrasensitive photodetectors based on monolayer MoS₂. *Nat. Nanotechnol.* **8**, 497–501 (2013).
36. Lee, S., Jung, S. W., Park, S., Ahn, J., Hong, S. J., Yoo, H. J. & Cho, D. I. D. Fabrication and evaluation of silicon nanowire photodetectors on flexible substrate for retinal prosthetic system. *Sens. Mater.* **24**, 205–220 (2012).
37. Choi, W., Cho, M. Y., Konar, A., Lee, J. H., Cha, G. B., Hong, S. C. & Kim, S. High-detectivity multilayer MoS₂ phototransistors with spectral response from ultraviolet to infrared. *Adv. Mater.* **24**, 5832–5836 (2012).
38. Yin, Z., Li, H., Li, H., Jiang, L., Shi, Y., Sun, Y. & Zhang, H. Single-layer MoS₂ phototransistors. *ACS Nano* **6**, 74–80 (2011).
39. Sekine, T., Fukuda, K., Kumaki, D. & Tokito, S. The effect of mechanical strain on contact resistance in flexible printed organic thin-film transistors. *Flex. Print. Electron.* **1**, 035005 (2016).
40. Michel, M., Biswas, C., Tiwary, C., Saenz, G., Hossain, R., Ajayan, P. & Kaul, A. B. A thermally-invariant, additively manufactured, high-power graphene resistor for flexible electronics. *2D Mater.* **4**, 025076 (2017).



Open Access This article is licensed under a Creative Commons Attribution 4.0 International License, which permits use, sharing, adaptation, distribution and reproduction in any medium or format, as long as you give appropriate credit to the original author(s) and the source, provide a link to the Creative Commons license, and indicate if changes were made. The images or other third party material in this article are included in the article's Creative Commons license, unless indicated otherwise in a credit line to the material. If material is not included in the article's Creative Commons license and your intended use is not permitted by statutory regulation or exceeds the permitted use, you will need to obtain permission directly from the copyright holder. To view a copy of this license, visit <http://creativecommons.org/licenses/by/4.0/>.

© The Author(s) 2017